Crystal growth at long times: Critical behavior at the crossover from diffusion to kinetics-limited regimes

Hartmut Löwen,
Sektion Physik der Universität München, Theresienstrasse 37, D-8000 München 2, Germany

John Bechhoefer
Department of Physics, Simon Fraser University, Burnaby, British Columbia, Canada V5A 1S6

Laurette S. Tuckerman
Department of Mathematics and Center for Nonlinear Dynamics, University of Texas, Austin, Texas 78712
(Received 9 October 1991)

We simulate one-dimensional crystal growth from an undercooled melt using a phase-field model and find interesting behavior when the liquid is undercooled by L/c_p degrees ("unit undercooling"). L is the latent heat and c_p the specific heat. For smaller undercoolings, the diffusion of latent heat limits growth and the velocity of the solid-liquid interface decays with time as $t^{-1/2}$. For larger undercoolings, nonequilibrium interface kinetics limits growth, and the interface velocity is constant. At unit undercooling, there are two scenarios, depending on the ratio of order parameter to thermal diffusivity (p). If p is small, the front-decay velocity is very well described by a power law $t^{-\nu}$, with $\nu \approx 0.3$. If p is large, the velocity at unit undercooling is finite. The branch of steady-state solutions then extends to smaller undercoolings, where the solid created is superheated. At the end of the branch, the solution jumps to a $t^{-1/2}$ velocity-decay law. Although pure materials have small p's, impure materials can have large p's, so that the two scenarios at unit undercooling should be observable experimentally. Although our simulations apply strictly only to one-dimensional fronts, similar behavior is expected in two and three dimensions. The presence of the Mullins-Sekerka instability is unlikely to change our conclusions.

PACS number(s): 61.50.Cj, 68.45.−v, 05.70.Fh, 81.30.Fb

I. INTRODUCTION

Theoretical models of crystal growth from the melt have generally considered two limits. In "order-parameter models," an equation is given for a nonconserved "crystallinity" order parameter [1,2]. The temperature field is assumed to be uniform and constant, meaning that temperature variations due to the release of latent heat produced by freezing are ignored. Order-parameter models account for various microscopic properties of the solidification process, such as the finite width of the solid-liquid interface, the kinetic time scale governing the dynamics of fluctuations, and the deviations from thermodynamic equilibrium that drive the interface forward. They typically predict that planar fronts will propagate at a constant velocity v that is proportional to the undercooling.

By contrast, in "diffusion models," the basic variable is the temperature field [3,4]. Although the release and subsequent diffusion of latent heat are both properly accounted for, the various microscopic features of the order-parameter models are ignored: the interface is assumed to be sharp and in local equilibrium. (A variant of the diffusion models introduces a phenomenological interface undercooling that varies linearly with the velocity. See Sec. II B, below.) In contrast with the first kind of model, steady-state motion is in general impossible. Indeed, dimensional analysis suggests that the typical asymptotic state has a front velocity that decays with time as $t^{-1/2}$.

The above models can be generalized by coupling an order parameter to the temperature field. This "phase-field" model of Halperin, Hohenberg, and Ma [5,6] (their "model C") originally included stochastic terms. Its deterministic version was studied, around 1985, in the context of crystal growth by Collins and co-workers [7,8] and Langer [9], and by Caginalp [10]. Liu and Goldenfeld used an approximate discretization of the phase-field equations to study crystal growth at long times [11]. (Their viewpoint is rather different from the one that will be adopted here.) Recently, the same model was examined in more detail by Schofield and Oxtoby [12], as well as the current authors [13,14]. The interest in this more detailed model is that it describes both diffusion- and kinetics-limited front motion in a single set of coupled equations. There are also new effects, not predicted by either of the simpler models, that should be experimentally observable.

The paper is organized as follows. In Sec. II we define two versions of the phase-field model and review what is known about its solutions and how they compare with the predictions of simpler models. The numerical techniques used to solve the equations of motion are described in Sec. III. In Sec. IV we discuss our results for the long-time behavior of the interface velocity as a function of liquid undercooling and of materials parameters. We digress in Sec. V to show how long-range forces and conserved order-parameter dynamics influence the motion of fronts. In Sec. VI we discuss the most likely candidates for observing experimentally the qualitatively

new phenomena predicted by the phase-field model. Conclusions are given in Sec. VII.

II. THE PHASE-FIELD MODEL

A. Basic equations

The phase-field model couples the dynamics of a nonconserved order parameter to those of a temperature field. It describes crystal growth into an undercooled liquid melt and accounts for the release and subsequent diffusion of latent heat. In this paper we will restrict ourselves to a one-dimensional, infinite geometry described by a spatial coordinate z. The order-parameter field $m(z,t)$ represents, for example, the amplitude of a Fourier component of the density field describing the crystalline lattice. It is zero in the liquid and may be scaled to be one in the solid at the solid-liquid coexistence temperature T_0. The temperature field $T(z,t)$ can also be scaled to be dimensionless by L/c_p, where L is the latent heat of fusion per mole and c_p is the specific heat at constant pressure. The dimensionless-undercooling field, then, is $u(z,t)=c_p[T(z,t)-T_0]/L$. If one considers a solid front advancing into a liquid held at a temperature $u=-\Delta$, the latent heat released is just enough to transform the undercooled liquid into solid at the coexistence temperature when $\Delta=1$. If $\Delta<1$, then excess heat must be transported away from the interface. If $\Delta>1$, the growing solid will be cooler than it would be at coexistence with the liquid.

The equation of motion for the dimensionless temperature field $u(z,t)$ is

$$\frac{\partial u}{\partial t}=D_T\frac{\partial^2 u}{\partial z^2}+\frac{\partial m}{\partial t} \ . \tag{1}$$

Here, D_T is the thermal diffusivity, assumed to be identical in both phases and independent of the temperature. Equation (1) describes the diffusion of heat, with the $\partial m/\partial t$ term acting as a source for the heat field.

In the Ginzburg-Landau approach, the equation of motion for the order-parameter field $m(z,t)$ is given by

$$\frac{\partial m}{\partial t}=-\Gamma\frac{\delta F[m,u]}{\delta m} \ . \tag{2}$$

Here, $F[m,u]$ is the dimensionless free-energy functional for the order parameter m at temperature u. The free energy is scaled by $\lambda k_B T_0 A/V$, where A is the cross-sectional area of the interface, V is the system volume, and λ is an energy, in units of $k_B T_0$, that may be related to the solid-liquid surface tension. For $u=0$, F has two equal minima at $m=0$ and $m=1$. Γ is an Onsager coefficient, which sets the microscopic time scale for order-parameter relaxation and is assumed to be independent of m and u. With the above scaling, F is given by

$$F[m,u]=\int_{-\infty}^{\infty}dz\left[\frac{1}{2}\xi_m^2\left(\frac{\partial m(z,t)}{\partial z}\right)^2+f(m(z,t),u(z,t))\right] \tag{3}$$

where ξ_m is the microscopic bulk correlation length. The local free-energy density $f(m,u)$ is

$$f(m,u)=f_0(m)+\tfrac{1}{2}\delta u m \tag{4}$$

where $f_0(m)$ is the local free-energy density at coexistence and $\frac{1}{2}\delta u m$ is the first term in a temperature expansion around $T=T_0$. (The factor $\frac{1}{2}$ is introduced to be consistent with the notation used in previous work [7,12–14].) The coefficient $\frac{1}{2}\delta$, which couples m to u, is derived by requiring that

$$L=T_0(\Delta S)=T_0(S_{\rm liq}-S_{\rm sol})=T_0\left[\left.\frac{\partial F}{\partial T}\right|_{\rm liq}-\left.\frac{\partial F}{\partial T}\right|_{\rm sol}\right] \tag{5}$$

where S is the entropy. Taking into account the scalings for F and u, we have

$$\delta=\frac{2}{\lambda}\frac{L}{k_B T_0}\frac{L}{c_p T_0} \ . \tag{6}$$

The local free-energy density $f_0(m)$ must have equal quadratic minima at $m=0$ and 1. In this paper, we consider two different forms for $f_0(m)$ that have this property. In the *Ginzburg-Landau model,* $f_0(m)$ is defined by the quartic polynomial

$$f_0(m)=m^2(m-1)^2 \ . \tag{7}$$

In the *parabolic model,* $f_0(m)$ is defined by a piecewise-parabolic function

$$f_0(m)=\tfrac{1}{2}\min[m^2,(m-1)^2] \ . \tag{8}$$

The two models have the same qualitative behavior: The Ginzburg-Landau potential is smoother and presumably somewhat more realistic, while the parabolic model has a piecewise-linear equation of motion for m that allows a partial analytic treatment [13].

We next define microscopic order-parameter length and time scales. The length scale is $z_m\equiv\sqrt{2}\xi_m$. (The $\sqrt{2}$ is for consistency with the notation used in previous work [12].) The time scale is $\tau_m\equiv 1/\Gamma$, leading to velocity and acceleration scales, $v_m=z_m/\tau_m$ and $a_m=z_m/\tau_m^2$. Rescaling Eqs. (1) and (2), we have

$$u_t=\frac{1}{2p}u_{zz}+m_t \ , \tag{9}$$

$$m_t=\tfrac{1}{2}m_{zz}-\frac{df_0}{dm}-\frac{\delta u}{2} \ . \tag{10}$$

Materials properties are now described solely by two dimensionless parameters, δ and p, where

$$p\equiv\frac{\xi_m^2/\tau_m}{D_T} \ . \tag{11}$$

Note that ξ_m^2/τ_m can be interpreted as an order-parameter diffusion constant, denoted D_m, so that $p=D_m/D_T$.

To fix the boundary conditions, we need to know four values: $m_\pm\equiv m(\pm\infty,t)$ and $u_\pm\equiv u(\pm\infty,t)$. We first require local equilibrium at $z=\pm\infty$, which gives two equations relating $m_\pm$ and $u_\pm$:

$$\left.\frac{df_0}{dm}\right|_{m_\pm} = -\frac{\delta}{2}u_\pm \ . \tag{12}$$

We obtain the other two equations by fixing the temperature at $z=\pm\infty$, so that $u_\pm=-\Delta$. One would then study the growth of a solid germ that has nucleated at $z=0$. We obtain $m_\pm$ by solving the algebraic equation (12). For the parabolic model, (12) is a linear equation; for the Ginzburg-Landau model, it is a cubic equation, the physically significant root of which is the one closest to zero. The temperature of the solid that is created is fixed by the equations themselves.

For numerical convenience, we also considered "steady-state" boundary conditions, where a semi-infinite amount of solid has already been created. We retain $u_+=-\Delta$ but adopt conditions at $z=-\infty$ that specify the state of the solid. One can show that for constant-velocity fronts [12],

$$u_+ - m_+ = u_- - m_- \ . \tag{13}$$

Along with (12), (13) suffices to fix $u_\pm$ and $m_\pm$.

We also considered "coexistence" boundary conditions, where we took, in place of (13),

$$u_-=0 \ , \quad m_-=1 \ . \tag{14}$$

In this case, the solid is created at equilibrium. For a unique undercooling Δ_c, both the steady-state and coexistence boundary conditions are identical. For $\delta\to 0$, one has $\Delta_c=1$.

In the phase-field model, the δu term implies that the m value of the minimum of the liquid depends slightly on the undercooling via (12). In particular, m will be positive in the metastable liquid phase if the liquid is undercooled. This means that Δ_c is slightly smaller than 1 and is a function of δ. If the order parameter is associated with crystallinity, this feature of the phase-field model is artificial, since crystallinity is in fact zero in a liquid, even when undercooled. The δ dependence of Δ_c results from our simple choices for the free energy $f(m,u)$ and does not affect qualitatively our conclusions. In addition, one can define m to be a combination of both crystallinity and density, in which case the dependence of m and Δ_c on δ in an undercooled liquid is real. Since for $\Delta=\Delta_c$, the amount of heat generated by freezing is just enough to heat the liquid back up to the coexistence temperature, we refer to this as *unit undercooling*. Explicitly, combining Eqs. (12) and (14), we find for the Ginzburg-Landau model (7) that

$$\Delta_c = 1 - \frac{(1-\sqrt{1-2\delta})}{4} \ . \tag{15}$$

In the parabolic model (8), one finds

$$\Delta_c = \frac{1}{1+\frac{1}{2}\delta} \ . \tag{16}$$

One can easily understand physically, even at this early stage, why one expects to see different kinds of freezing behavior for small undercoolings ($\Delta<\Delta_c$) and for large undercoolings ($\Delta>\Delta_c$). In the former case, let us start with an entirely liquid sample. Then imagine that it is all converted to solid without the latent heat's diffusing anywhere. The release of latent heat raises the temperature by Δ_c (i.e., by approximately L/c_p in real units). This temperature rise, however, exceeds the undercooling that the liquid originally had. Were the heat truly to stay put and not diffuse, then the solid created would be superheated. The true equilibrium, in fact, requires that some of the heat be transported away to infinity and that the solid be at the coexistence temperature. Since the transport of heat to infinity is via diffusion, one naively expects diffusive scalings for the front position, velocity, etc., and thus it is not surprising that we find that the front in this case slows down via a power law of the form $v(t)\propto t^{-1/2}$.

By contrast, if $\Delta>\Delta_c$, the heat is not sufficient to raise the temperature of the solid back up to coexistence. The solid is then below its coexistence temperature, a thermodynamically stable situation. Since no heat need be transported out to infinity, solidification is limited only by the kinetics of transforming liquid to solid, and fronts travel at constant velocity.

The case $\Delta=\Delta_c$, where the latent heat is just enough to reheat the solid back to T_0 is a special point that divides the diffusion-limited from the kinetics-limited regimes. Below, we shall show that the phase-field model predicts two types of behavior at Δ_c, depending on p.

Finally, we must set the initial conditions for m and u. For the germ, we choose either Gaussian or quasi-sharp-kink profiles. (See Figs. 12 and 13.) For steady-state and coexistence boundary conditions, we start from a tanh-like profile. (See Fig. 3.) We define these profiles in Sec. III. Apart from the initial transient, the results were independent of the details of both the initial conditions and the boundary conditions.

B. Review of previous results and open questions

The original interest in the phase-field model for crystallization came mainly from an inadequacy of the purely diffusive model, with its sharp interface held at local equilibrium $u=0$. This model implies that for $\Delta<1$, fronts slow down via a $t^{-1/2}$ power law [15]. For $\Delta>1$, the model has no solution. The latent heat will increase the temperature of the solid by 1 at most; this is inconsistent with the requirement that $u=0$ at the interface. At $\Delta=1$, the front will travel at a constant but indeterminate velocity [4]. Although there are three qualitatively different regimes in this model, the model breaks down when $\Delta\geq\Delta_c=1$. For $\Delta\ll\Delta_c$, however, it is perfectly satisfactory.

The diffusive model may be improved by adding a phenomenological description of kinetics. Instead of assuming that the solid-liquid interface is at $T_i=T_0$, one sets the interface temperature to $T_i=T_0-\beta^{-1}v$, where v is the interface velocity and β is known as a kinetic coefficient [3,16,17]. In this model, fronts with $\Delta<1$ slow down via a $t^{-1/2}$ power law, as before. For $\Delta>1$, fronts travel at constant velocity $v\propto(\Delta-1)$. The model thus gives sensible results for both $\Delta<\Delta_c$ and for $\Delta>\Delta_c$, where here $\Delta_c=1$ [3].

For $\Delta=\Delta_c$, Oswald [18] has recently argued that

$v(t) \propto t^{-1/3}$. We reproduce here his argument: Consider a germ of radius R and volume proportional to R^d, where d is the spatial dimension. The amount of latent heat released in solidifying out to a radius R is

$$R^d L = R^d[c_p(T_i - T_\pm)] + R^{d-1}(D_T/v)[c_p(T_i - T_\pm)] \tag{17}$$

where $T_\pm$ is the temperature at infinity. In (17), the left-hand side is proportional to the total latent heat released. The first term of the right-hand side is proportional to the amount of heat retained to warm up the solid to coexistence. The second term approximates the amount of heat rejected into the liquid phase. Using $\Delta = (T_0 - T_\pm)/(L/c_p)$, Eq. (17) may be nondimensionalized to read

$$1 - \Delta - \frac{T_i - T_0}{L/c_p} = \frac{D_T}{Rv}\Delta + \frac{T_i - T_0}{L/c_p} \ . \tag{18}$$

In the diffusion model, the interface is at the coexistence temperature, and so the term $(T_i - T_0)/(L/c_p)$ is zero; this is satisfactory as long as $\Delta \ll 1$. Setting $v = dR/dt$ and integrating (18) then gives the usual law $R(t) \propto t^{-1/2}$ [13]. When $\Delta = 1$, the diffusion model breaks down; the kinetic correction $T_i - T_0 \approx \beta^{-1} v$ remains negligible in the right-hand side of (18) but dominates in the left-hand side, leading to

$$\frac{v}{\beta(L/c_p)} = \frac{D_T}{Rv} \ . \tag{19}$$

Integrating (19), we obtain $v \propto [D_T(L/c_p)\beta]^{1/3} t^{-1/3}$, as claimed. The $\frac{1}{3}$ exponent is an explicit consequence of the global conservation of the latent heat released during solidification.

The phase-field model provided another solution to the velocity-degeneracy problem of the pure diffusion model. Both Langer [9] and Collins and Levine [7] showed that the phase-field model has a unique, constant-velocity solution at unit undercooling that is selected by microscopic order-parameter kinetics. The lack of such microscopic length and time information leads to the velocity degeneracy in the diffusive model.

The phase-field model reduces to the diffusive model with linear kinetics when $\delta \to 0$ and $p/p_c \to 0$, where the order-parameter profile becomes essentially a step function and the heat or impurity field obeys the standard (uncoupled) diffusion equation [9,7,10]. The most thorough discussion is by Caginalp [19]. The phase-field model also has numerical advantages in the modeling of the complex, dendritic patterns that arise during solidification in two- and three-dimensional geometries [20].

Schofield and Oxtoby have recently found that the $\Delta = \Delta_c$ steady-state solutions to the phase-field model discovered by Langer [9] and Collins and Levine [7] exist only for certain values of the material parameters p and δ. In particular, for $p < p_c(\delta)$, there are no steady-state solutions. They evaluated p_c perturbatively for small δ in the Ginzburg-Landau model and found $p_c = 2/(3\delta)$. Löwen, Schofield, and Oxtoby [13] then repeated the calculations of Schofield and Oxtoby for the parabolic model (8) and found similar results. In the parabolic model, various quantities can be calculated analytically. For example, $p_c(\delta)$ is exactly $2/(3\delta)$.

Finally, two of us explored the effect of different values of Δ in the parabolic model [14]. For very large couplings δ, we showed that there is a critical point in δ-p-Δ parameter space, giving rise to different velocity scalings in $\Delta - \Delta_c$. As $\Delta - \Delta_c \to 0$, there is a transition from steady-state growth to the diffusive regime. At Δ_c, v remains nonzero for $p > p_c$. Otherwise, v vanishes as $(\Delta - \Delta_c)^\nu$ with $\nu = 1$ for $p < p_c$, $\nu = 1/2$ for $p = p_c$, and $\nu = 1/3$ for $p = p_c$ and $\delta = \delta_c \equiv \frac{4}{3}$.

The current work, then, was motivated by several unanswered questions: Does the phase-field model reproduce the velocity-decay laws seen in the diffusive models? What experiments have been or could be done? In the constant-velocity regime, how are steady-state solutions approached? Are they stable (at least in one dimension)? If both steady-state and decaying-velocity solutions exist at $\Delta = \Delta_c$, when is each to be seen? Is the exponent of $1/3$ predicted by Oswald independent of p and δ? We would also like to explore the jump in velocity just below Δ_c for $p > p_c$ that was discussed in [14]. Finally, what are the effects of long-range forces? What happens if the order parameter is conserved?

C. Application of the phase-field model to alloys

It has long been realized within the metallurgical community that the equations of motion describing the freezing of a metal alloy are similar to the ones describing the freezing of a pure material [21]. In practice, even nominally pure materials usually contain enough impurities that mass diffusion—and not that of latent heat—limits crystal growth. For brevity, we shall refer to the second component of an alloy as an impurity, whether or not it is deliberately added. Since impurities are usually segregated preferentially in the liquid phase, a moving solid-liquid front is a source of impurities as well as latent heat. If there are enough impurities, one may neglect the accompanying diffusion of latent heat [17]. We shall use this approximation in our discussion of chemical effects. Langer showed that by considering the chemical potential rather than the concentration field, the chemical version of the diffusion model can be mapped exactly onto those for the thermal version [22].

To generalize Langer's method to the phase-field model, we define a dimensionless chemical potential of impurities in analogy with the dimensionless temperature field defined above. Thus

$$u(z,t) = \frac{T - T_0}{L/c_p} \to \frac{\mu - \mu_0}{\Delta C(\partial\mu/\partial C)} \tag{20}$$

where μ_0 is the chemical potential at which the solid and liquid coexist. ΔC is the equilibrium concentration jump across the interface and is analogous to the latent heat L. (See Fig. 1.) Thus, $\Delta C(\partial\mu/\partial C)$ sets the natural scale for variations of the chemical potential, just as L/c_p does in the thermal case. Assuming that the liquidus and solidus phase boundaries are straight lines, as depicted in Fig. 1,

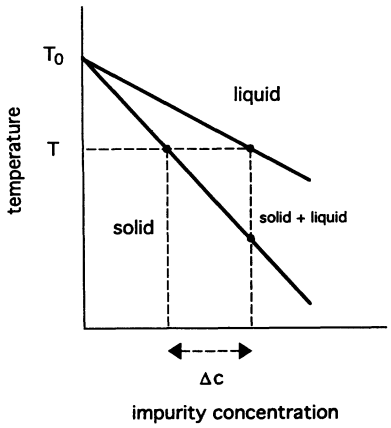

FIG. 1. Temperature-impurity phase diagram showing the equilibrium jump in impurity concentration, ΔC, across the solid-liquid interface at a temperature T. The heavy lines represent the liquidus and solidus curves, which separate the liquid and solid regions from the two-phase coexistence region, respectively.

ΔC may be evaluated in terms of the liquidus slope dT/dC and the ratio of liquidus to solidus slopes k. The ratio k is known as the equilibrium partition coefficient and is a measure of how much impurities are segregated into the liquid phase. In Fig. 1, we have $k<1$. The strength of the "impurity source" is

$$\Delta C=\frac{T_0-T}{dT/dC}(1-k) . \tag{21}$$

Note that ΔC depends on temperature, in contrast to the latent heat in the thermal model, which is a fixed materials parameter. In the chemical case, ΔC is varied by changing the temperature at which one chooses to work. (Recall that we are assuming that the solidification is isothermal.)

Referring to Fig. 1 once more, we can understand qualitatively the effect of changing the solidification process. Assume that the system is entirely liquid, with an impurity concentration of C_0 and a temperature of $T_0-(C_0dT/dC)$. In other words, the system is sitting just on the liquidus line. Now quench the temperature. If the temperature is quenched to a value somewhere between the liquidus and solidus (slicing vertically at $C=C_0$), then in a finite box, the end state will be liquid and solid in coexistence, with the fraction of liquid determined by the depth of the quench. If the temperature is quenched to the solidus temperature $T_0-(C_0dT/dC)/k$, then the end state will be a solid at equilibrium (because the system will be sitting at the solidus). If the temperature is set below the solidus, the end state will be a stable solid that is cooled below the solid-liquid coexistence temperature.

The quench from liquidus to solidus thus defines unit undercooling, and the temperature scale becomes

$$\frac{L}{c_p}\rightarrow C_0\frac{dT}{dC}\frac{1-k}{k} . \tag{22}$$

Two differences, however, should be noted. In the thermal case, one controls the temperature by setting boundary conditions for u. In the chemical case, proceeding analogously would imply fixing the value of the chemical potential at infinity. In practice, one fixes the temperature instead. This will simultaneously change the scale of u and the values of δ and p/p_c. A second difference is that in the thermal case, when $\Delta<\Delta_c$, the entire liquid is solidified, whereas in the chemical case, the result is a mixture of liquid and solid, with the relative proportions fixed by the depth of the quench. The difference stems from the boundary conditions: In the thermal case, one fixes the temperature, so that energy is transported out of the system into a surrounding heat bath. In the chemical case, the sample is usually encased in a box that is impervious to the diffusion of impurities. The boundary condition then is that the derivative of u is zero. If the total amount solidified is much less than the equilibrium solid fraction at the chosen temperature quench, then there is no difference between the thermal and chemical cases. Experimentally, this situation is easy to realize. All of these subtleties affect the coefficients and the boundary conditions of the equations of motion, but they do not change the form of the equations themselves.

In order to evaluate δ in the chemical model, we write the analog of Eq. (5), with $T\rightarrow\mu$ and $S\rightarrow C$. The jump in entropy at the solid-liquid interface corresponds to the impurity jump depicted in Fig. 1. We have then

$$\Delta C=\left.\frac{\partial F}{\partial\mu}\right|_{\rm liq}-\left.\frac{\partial F}{\partial\mu}\right|_{\rm sol}=\lambda k_B T_0\frac{\delta}{2}\frac{1}{(\partial\mu/\partial C)(\Delta C)} . \tag{23}$$

Noting that

$$\frac{\partial\mu}{\partial C}=\frac{dT}{dC}\frac{L}{T_0\Delta C} \tag{24}$$

(see [20], footnote 4 on p. 9) and using Eq. (21), we have

$$\delta=\frac{2}{\lambda}\frac{L}{k_B T_0}\frac{T_0-T}{T_0}(1-k) . \tag{25}$$

Notice that the temperature dependence of ΔC implies that the coupling constant δ may be varied by changing the overall concentration of impurities in the material being studied. (One could achieve similar effects in the thermal model by varying the pressure at which the solidification occurs, since one then expects the latent heat L to vary.) At unit undercooling,

$$\delta=\frac{2}{\lambda}\frac{L}{k_B T_0}\frac{C_0dT/dC}{T_0}\frac{1-k}{k} . \tag{26}$$

The other material parameter, p, is given by

$$p=\frac{D_m}{D_C} \tag{27}$$

where D_C is the impurity mass diffusion constant.

In summary, with the above assignments for u, δ, and p, the equations of motion are exactly the same as given in Eqs. (9) and (10), above. As discussed below, the values of δ and p will be significantly different for

impurity-driven systems; there is also the attractive possibility of tuning δ.

III. NUMERICAL TECHNIQUES

Here, we detail our numerical methods for solving the Ginzburg-Landau and parabolic versions of the phase-field model. Because some of the techniques we use are not straightforward and because they are necessary to follow solutions out to the long times we are interested in, we present them in some detail; however, readers interested mainly in the behavior of the solutions rather than in the methods for obtaining them can safely skip this section.

A. Ginzburg-Landau model

In this section, we describe an adaptive-grid technique for integrating the coupled system of partial differential equations:

$$u_t=\frac{1}{2p}u_{zz}+\tfrac{1}{2}m_{zz}-4m(m-\tfrac{1}{2})(m-1)-\tfrac{1}{2}\delta u \ , \tag{28}$$

$$m_t=\tfrac{1}{2}m_{zz}-4m(m-\tfrac{1}{2})(m-1)-\tfrac{1}{2}\delta u \ . \tag{29}$$

Direct numerical integration of (28) and (29) over long times is complicated by two features of the solutions [12].

(1) The solution profiles are steep fronts, whose spatial variation is extremely localized.

(2) Although the shapes of these fronts vary little over time, the fronts move at a velocity which is neither known nor constant: indeed, this is the crux of our investigation.

The first problem is easily resolved by using an unequally spaced grid of points $z^{(j)}$, $j=-N/2,\ldots,0,\ldots,N/2$, such that

$$\tanh(z^{(j)}/z^{(\max)})=2j/N \ . \tag{30}$$

Effectively, this choice of grid is equivalent to mapping the real line $(-\infty,+\infty)$ to the interval $[-1,+1]$ on which a uniform grid is used. The two quantities $z^{(\max)}$ and N can be varied independently, to represent fronts of different expected widths and steepness. The grid spacing (30) is commonly used in hydrodynamics, for example, in the study of mixing layers [23].

To deal with the second problem, we have used a *moving* grid which adapts *dynamically* to the solution profiles. To explain the adaptive-grid approach, we consider a general reaction-diffusion equation for a single field $c(z,t)$:

$$c_t(z,t)=g(c(z,t))+c_{zz}(z,t) \ . \tag{31}$$

Introducing a new variable ζ related to z by the inverse transformation $z=z(\zeta,t)$, we can formally define $C(\zeta,t)\equiv c(z(\zeta,t),t)$ and derive from (31) the equation governing the evolution of $C(\zeta,t)$:

$$C_t=g(C(\zeta,t))+\frac{1}{z_\zeta^2}C_{\zeta\zeta}+\left[\frac{z_t}{z_\zeta}-\frac{z_{\zeta\zeta}}{z_\zeta^3}\right]C_\zeta \ . \tag{32}$$

We now specialize to two forms for the change of coordinates $z(\zeta,t)$, namely, a translating frame:

$$z(\zeta,t)=\zeta+\phi(t) \tag{33}$$

and a dilating frame:

$$z(\zeta,t)=\zeta\psi(t) \ . \tag{34}$$

Our goal is to choose $\phi(t)$ or $\psi(t)$ in such a way that the fronts remain near the origin of our new coordinate system, i.e., near $\zeta=0$, where the grid points are densely placed according to (30). We will do this by deriving differential equations for ϕ and ψ. Initially, the moving frame will coincide with the stationary ("laboratory") frame, i.e., $z(\zeta,0)=\zeta$. This is accomplished by specifying the initial conditions, $\phi(0)=0$ and $\psi(0)=1$.

The front position $z_0(t)$ can be defined such that $c(z_0(t),t)=\bar{c}$, where $\bar{c}$ is some specified threshold value contained in the range of $c(z,t)$. [If there is more than one front, define $z_0(t)$ to be the rightmost one.] In terms of our new coordinate, we define the front position via $C(\zeta_0(t),t)=\bar{c}$, and it is easily seen that $z_0(t)=z(\zeta_0(t),t)$. Our goal then is to enforce $\dot{\zeta}_0(t)=0$.

In the translating frame (33), since $z_\zeta=1$, $z_{\zeta\zeta}=0$, and $z_t=\phi_t$, (32) becomes

$$C_t=g(C(\zeta,t))+C_{\zeta\zeta}+C_\zeta\phi_t(t) \ . \tag{35}$$

If $\phi(t)=vt$, Eq. (35) reduces to the usual transformation to a frame moving at constant velocity v. More generally, by setting

$$\phi(t)=\int_0^t\dot{z}_0(t')dt' \ , \tag{36}$$

we enforce $\dot{\zeta}(t)\approx 0$. The integrand of (36) is determined dynamically during the course of the integration via the threshold criterion and the transformation (33).

In the dilating frame (34), we have $z_\zeta=\psi$, $z_{\zeta\zeta}=0$, and $z_t=\zeta\psi_t$ and Eq. (32) becomes

$$C_t=g(C(\zeta,t))+\frac{1}{\psi^2}C_{\zeta\zeta}+\frac{\zeta\psi_t}{\psi}C_\zeta \ . \tag{37}$$

Since definition (34) now implies that

$$\dot{z}_0(t)=\zeta_0\dot{\psi}+\dot{\zeta}_0\psi \tag{38}$$

in order to enforce $\dot{\zeta}_0\approx 0$, we set

$$\psi(t)=\int_0^t\frac{1}{\zeta_0(t')}\dot{z}_0(t')dt' \ , \tag{39}$$

where the integrand of (39) is again determined dynamically.

The transformations leading to (32) can be performed entirely analogously on the coupled system (28) and (29) by replacing

$$\partial_{zz}\rightarrow\frac{1}{z_\zeta^2}\partial_{\zeta\zeta}-\frac{z_{\zeta\zeta}}{z_\zeta^3}\partial_\zeta \ , \tag{40}$$

$$\partial_t\rightarrow\partial t-\frac{z_t}{z_\zeta}\partial_\zeta \ . \tag{41}$$

In the translating two-variable case, the resulting three coupled differential equations are

$$U_t=\frac{1}{2p}U_{\zeta\zeta}+\tfrac{1}{2}M_{\zeta\zeta}-4M(M-\tfrac{1}{2})(M-1)-\frac{\delta}{2}U+\phi_t U_\zeta\ , \tag{42}$$

$$M_t=\tfrac{1}{2}M_{\zeta\zeta}-4M(M-\tfrac{1}{2})(M-1)-\frac{\delta}{2}U+\phi_t M_\zeta\ , \tag{43}$$

$$\phi_t=\dot{z}_0\ , \tag{44}$$

while in the dilating two-variable case they are

$$U_t=\frac{1}{\psi^2}\left[\frac{1}{2p}U_{\zeta\zeta}+\tfrac{1}{2}M_{\zeta\zeta}\right]-4M(M-\tfrac{1}{2})(M-1)-\frac{\delta}{2}U+\frac{\zeta\psi_t}{\psi}U_\zeta\ , \tag{45}$$

$$M_t=\frac{1}{\psi^2}\frac{1}{2}M_{\zeta\zeta}-4M(M-\tfrac{1}{2})(M-1)-\frac{\delta}{2}U+\frac{\zeta\psi_t}{\psi}M_\zeta\ , \tag{46}$$

$$\psi_t=\frac{1}{\zeta_0}\dot{z}_0\ . \tag{47}$$

For the translating case, we use the steady-state and coexistence boundary conditions. (See Sec. II A.) Note that formula (30) includes grid points that are actually at the boundaries, i.e., $z^{(-N/2)}=\zeta^{(-N/2)}=-\infty$ and $z^{(N/2)}=\zeta^{(N/2)}=+\infty$ and that these points are used in the computations in both of the adaptive frames. The initial profile is a smooth, tanh-like interpolation between the boundary values $m_-\equiv m(-\infty,t)$ and $m_+\equiv m(+\infty,t)$,

$$m(z,t=0)=m_+ +\frac{m_- -m_+}{1+e^{z/a}} \tag{48}$$

and similarly for u, where the width $a=0.8$. The front is defined to satisfy $m(z_0(t),t)=(m_+ +m_-)/2$.

For the dilating frame, we use localized-germ boundary conditions. The initial profiles are Gaussians:

$$m(z,t=0)=m_+ +Ae^{-(z/a)^2} \tag{49}$$

and similarly for u, with widths of $a=1.5$ or 2. A is taken to be 1 for m and 1.2 for u. The position of the front in the dilating Gaussian case is defined to be the rightmost point z_0 satisfying $m(z_0(t),t)=\frac{1}{2}$.

To integrate system (42)–(44), we use Crank-Nicolson time stepping to propagate the second derivative (diffusive) terms $U_{\zeta\zeta}$ and $M_{\zeta\zeta}$, which, as in [12], requires solving a septadiagonal matrix equation. To propagate the remaining terms, i.e., the algebraic terms in U and M, the first derivative terms in U_ζ and M_ζ, and the $\dot{z}_0$ term in (44), we used the Adams-Bashforth approximation to the time derivative. Spatial derivatives were computed via second-order-accurate finite difference formulas which use the spacing (30). Local cubic interpolation at the m front was necessary to determine the threshold $\zeta_0(t)$ to sufficiency accuracy.

The combined semi-implicit scheme is second-order accurate in time. Empirically, we found that the time step is limited by accuracy rather than by stability, to $\Delta t\approx 0.4$, and this is the value used for most of our runs. The computation time scales approximately linearly with the number N of grid points. Each time step takes about 2×10^{-4} CPU sec per grid point on a Sun Sparc Station 1 system and 2×10^{-6} CPU sec per grid point on a Cray YMP8-864 system.

The dilating frame equations (45)–(47) were integrated similarly, except that backwards Euler time stepping was used for the diffusive terms and forwards Euler for the remaining terms, resulting in a first-order-accurate semi-implicit scheme. Since in this case, the diffusive operator contains the time-varying factor $1/\psi^2$, the septadiagonal matrix must be recomputed (and factored into lower and upper triangular matrices for inversion) at each step, resulting in considerably greater expense than the translating frame simulations. The explicitly propagated terms pose a more stringent stability criterion on the time step ($\Delta t\approx 0.05$) than those of the translating frame, leading to a smaller time step. In addition, the dilating frame fails to use the grid spacing (30) as efficiently as the translating frame, for which the grid points are concentrated precisely in the only nonconstant region of the profiles. With sufficient spatial and temporal resolution, results from the translating and dilating simulations agree, justifying the less physically realistic steady-state and coexistence boundary conditions used with the translating frame.

A fundamental difficulty of the equations is that the u profile becomes broader over time, whereas the m profile remains sharp. For the translating frame, the domain size, measured by $2z^{(\max)}$, must be large enough to contain the widening u front, whereas the resolution, measured by the number N of spatial grid points, must be sufficiently fine to describe the steep m front. In practice, we imposed the criteria that (1) the width of the u front be no more than a sixth of the domain size, and that (2) the m front contain at least seven grid points. The minimal grid required depends on the properties of the solution and hence on the values of the parameters p and Δ and on the final time t. Most of the runs reported here used $z^{(\max)}=1000$ and $N=2000$; this was checked against simulations using a finer grid of $z^{(\max)}=2000$ and $N=8000$. (We used $z^{(\max)}=200$ and $N=1500$ for the dilating frame.) For low values of p, the u front diffuses slowly and $z^{(\max)}=300$ and $N=600$ provided sufficient resolution. For simulations in which the velocity decays to zero, the u front continues to widen over time, so that any value of $z^{(\max)}$ will eventually prove too small. For the dilating frame, the same problem presents itself differently: The domain expands in time so as to contain the entire germ and not merely the diffusing u front. The grid points become more widely spaced and eventually inadequate for describing the m front. This restricted the dilating frame simulations to much shorter times than the translating frame. This fundamental property of the equations implies that the simulations cannot be continued indefinitely without *separate* adaptive grid spacings for u and m.

B. The parabolic model

In the parabolic model, the scaled equations of motion for u and m are

$$u_t=\frac{1}{2p}u_{zz}+m_t\ , \tag{50}$$

$$m_t=\tfrac{1}{2}m_{zz}-m+\Theta(z+z_0(t))-\Theta(z-z_0(t))-\frac{\delta u}{2} \tag{51}$$

where the step functions $\Theta(z)$ result from the differentiation of $f(m)$ with respect to m and represent the slope discontinuity of the potential at the cusp [see Eq. (8)]. The interface position $z_0(t)$ is defined by

$$m(z_0(t),t)=\tfrac{1}{2} \tag{52}$$

which must be satisfied self-consistently [24,25].

In the following, we define $\bar{u}(z,t)=u(z,t)-u_0$ and $\bar{m}(z,t)=m(z,t)-m_0$, where $u_0=-1/(1+\delta/2)$ and $m_0=-\delta/2$. The equations of motion for $\bar{u}$ and $\bar{m}$ are the same as (50) and (51). They are linear equations with inhomogeneous terms involving z. For a given initial profile $\bar{u}(z,t_0)$, $\bar{m}(z,t_0)$, Eqs. (50) and (51) can be solved by Fourier transformation:

$$\begin{bmatrix}\bar{u}(z,t)\\ \bar{m}(z,t)\end{bmatrix}=\frac{1}{\sqrt{2\pi}}\int_{-\infty}^{\infty}dK\,e^{-iKz}\left[e^{\underline{C}_K(t-t_0)}\begin{bmatrix}\tilde{u}(K)\\ \tilde{m}(K)\end{bmatrix}+\left[\frac{2}{\pi}\right]^{1/2}\int_{t_0}^{t}dt'e^{\underline{C}_K(t-t')}\frac{\sin Kz_0(t')}{K}\begin{bmatrix}1\\1\end{bmatrix}\right] \tag{53}$$

where the initial profiles enter via

$$\begin{bmatrix}\tilde{u}(K)\\ \tilde{m}(K)\end{bmatrix}=\frac{1}{\sqrt{2\pi}}\int_{-\infty}^{\infty}dz e^{iKz}\begin{bmatrix}\bar{u}(z,t_0)\\ \bar{m}(z,t_0)\end{bmatrix}\equiv\mathbf{f}_K \tag{54}$$

and the 2×2 matrix $\underline{C}_K$ is given by

$$\underline{C}_K=-\begin{bmatrix}\frac{K^2}{2p}+\frac{\delta}{2} & \frac{K^2}{2}+1\\ \frac{\delta}{2} & \frac{K^2}{2}+1\end{bmatrix}. \tag{55}$$

The consistency requirement (52) then leads to an integral equation for $z_0(t)$:

$$\begin{aligned}\tfrac{1}{2}-m_0=(0,1)\cdot\frac{1}{\sqrt{2\pi}}\int_{-\infty}^{\infty}dK\,e^{-iKz_0(t)}&\times\left[e^{\underline{C}_K(t-t_0)}\begin{bmatrix}\tilde{u}(K)\\ \tilde{m}(K)\end{bmatrix}\right.\\&\left.+\left[\frac{2}{\pi}\right]^{1/2}\underline{F}_K(t)\begin{bmatrix}1\\1\end{bmatrix}\right]\end{aligned} \tag{56}$$

where the memory kernel is

$$\underline{F}_K(t)=\int_{t_0}^{t}dt'e^{\underline{C}_K(t-t')}\frac{\sin Kz_0(t')}{K}\ . \tag{57}$$

Starting from $z_0(t_0)$, Eq. (56) can be solved numerically by successive iteration. Once we have solved for $z_0(t)$, we can differentiate to find the interface velocity $v=dz_0/dt\equiv\dot{z}_0(t)$. The profiles of the order-parameter and temperature fields are obtained by inserting $z_0(t)$ into (53).

The initial field configurations are taken to be a differentiable combination of constant and parabolic functions that describe a quasi sharp kink. (See Figs. 12 and 13, below.)

$$\bar{u}(z,t_0)=\frac{1}{1+\delta/2}\begin{cases}1, & z\le L\\ 1-\frac{1}{2}(z-L)^2, & L<z\le L+1\\ \frac{1}{2}(z-L-2)^2\ , & L+1<z\le L+2\\ 0, & z>L+2\ ,\end{cases} \tag{58}$$

$$\bar{m}(z,t_0)=\bar{u}(z,t_0)\ , \tag{59}$$

$$L=4\ ,\quad z_0(t_0)=L+2-\left[\frac{1-2m_0}{|u_0|}\right]^{1/2}. \tag{60}$$

To iterate Eq. (56), the matrix $\underline{F}_K(t)$ must be updated each iteration step. Explicitly,

$$\begin{aligned}\underline{C}_K\underline{F}_K(t)=&-\frac{\sin Kz_0(t_0)}{K}\\&+e^{\underline{C}_K(t-t_0)}\frac{\sin Kz_0(t_0)}{K}+\underline{M}_K(t_0)\end{aligned} \tag{61}$$

where

$$\underline{M}_K(t_0)=\int_{t_0}^{t}dt'e^{\underline{C}_K(t-t')}\cos Kz_0(t')\dot{z}_0(t')\ . \tag{62}$$

The starting configuration is $z_0(t)=z_0(t_0)$, $\dot{z}_0(t')=0$, $\underline{M}_K(t_0)=\underline{0}$. The updated variables are

$$\dot{z}_0(t+\Delta t)=\frac{\frac{1}{2}+\int_0^{\infty}dK\cos Kz_0(t)(0,1)\cdot\left[\sqrt{2/\pi}\underline{C}_K e^{\underline{C}_K t}\mathbf{f}_K+(2/\pi)\underline{C}_K\underline{F}_K(t)\begin{bmatrix}1\\1\end{bmatrix}\right]}{\int_0^{\infty}dK\,K\sin Kz_0(t)(0,1)\cdot\left[\sqrt{2/\pi}e^{\underline{C}_K t}\mathbf{f}_K+(2/\pi)\underline{F}_K(t)\begin{bmatrix}1\\1\end{bmatrix}\right]}\ , \tag{63}$$

$$\underline{M}_K(t+\Delta t)=\underline{M}_K(t)e^{\Delta t\underline{C}_K}+\Delta t\cos Kz_0(t)\dot{z}_0(t)\underline{I}\ , \tag{64}$$

$$z_0(t+\Delta t)=z_0(t)+\Delta t\dot{z}_0(t+\Delta t)\ . \tag{65}$$

In (63), $\mathbf{f}_K$ is given by (54). After waiting approximately one time unit, the profiles were calculated. These served as the input for the next iteration, for which $\underline{M}_K$ was again set to zero to avoid an accumulation of errors in $\underline{M}_K(t)$.

The K integration was carried out on a grid of $N\approx 1000$ equally spaced points $K<K_{\max}=100$. This corresponds to a finite system of length $L\approx 350$, so that $z_0(t)\ll L$ for the times considered. The time step Δt is typically 0.000 01 to 0.0001, which is much smaller than that permitted by the adaptive-grid technique. However, because this integral-equation method is formulated in Fourier space, it can be easily generalized.

IV. RESULTS FOR THE LONG-TIME BEHAVIOR OF CRYSTAL-GROWTH VELOCITY

Figure 2 summarizes our main results: If the undercooling obeys $\Delta<\Delta_c$, then the velocity of the front decays via a $t^{-1/2}$ power law. For $\Delta>\Delta_c$, fronts propagate at a constant velocity. At $\Delta=\Delta_c$, there are two cases. For $p\le p_c$, the front velocity decays, with very nearly a power-law form $t^{-\nu}$ where the value of ν depends weakly on p and δ and for small δ is approximately 0.3. For $p>p_c$, the front propagates at a constant velocity at and even slightly below Δ_c (see below).

Figure 3 shows typical non-steady-state profiles. Those shown are at $\Delta=\Delta_c$, but the profiles for $\Delta<\Delta_c$ are similar. Our numerical techniques allow us to follow accurately the fronts out to times as large as 10^6 units. (Such runs consumed two CPU hours apiece on the Cray YMP computer.) Note that the order-parameter front width remains sharp, while the temperature field widens as the front slows down. By 10^6, the fronts closely resemble the shapes assumed in the diffusion models: a step function for m and an exponential-like decay for u with a kink at the interface position. What appear to be kinks in u in the figure are in fact smooth shapes at the microscopic length scale z_m and are well resolved by our grid. As can be seen clearly, the evolution of u from an initial sharp profile to an exponential-like decay involves a long transient. During the initial decay, the true long-time behavior is obscured. The slight bump on the m profiles results from the release of latent heat at the interface and corresponding change in the liquid order parameter. This

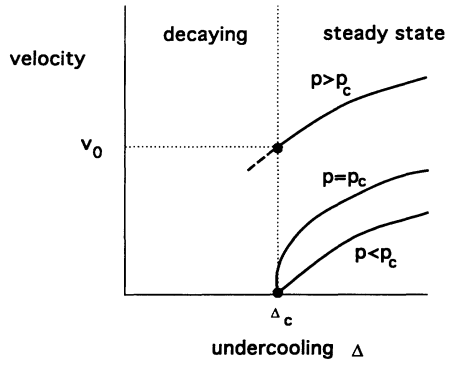

FIG. 2. Summary of the asymptotic behavior of the phase-field model. For undercooling $\Delta<\Delta_c$, fronts slow down with an asymptotic behavior $v(t)=At^{-1/2}$, whereas for $\Delta>\Delta_c$, fronts approach a steady-state velocity v exponentially: $v(t)=v+Ae^{-t/\tau_0}$. In the steady-state regime, there are three cases. If $p<p_c$, then near unit undercooling, the steady-state velocity is given by $v=A(\Delta-\Delta_c)$. If $p=p_c$, then $v=A(\Delta-\Delta_c)^{1/2}$. For $p>p_c$, the steady-state velocity is finite at Δ_c: $v=v_0+A(\Delta-\Delta_c)$. At Δ_c and $p\le p_c$, the velocity decay is significantly slower than a $t^{-1/2}$ power law and is well approximated by $v(t)=At^{-\nu}$, with $\nu\approx 0.3$. Finally, for $p>p_c$, there are steady-state solutions even for $\Delta<\Delta_c$, which are shown as a heavy dashed line. In the above, the constants A are different in each of the cases and depend on the material parameters p and δ.

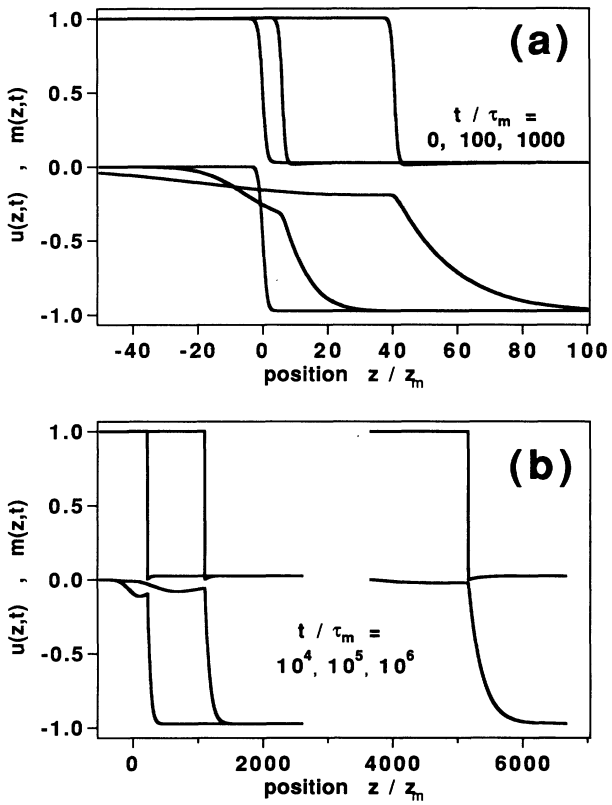

FIG. 3. Evolution of the order parameter $m(z,t)$ and heat field $u(z,t)$. The material parameters are $p/p_c=0.1$ and $\delta=0.1$. The undercooling $\Delta=\Delta_c$. In both (a) and (b), the upper curves denote m and the lower ones u. The horizontal positions of the different curves show the overall displacement of the front at times $t/\tau_m=0$, 100, and 1000 in (a) and $t/\tau_m=10^4$, 10^5, and 10^6 in (b). The z axis is scaled by z_m, the microscopic order-parameter length scale and the time by τ_m, the microscopic order-parameter time scale.

effect can also be seen in steady-state solutions [12,13].

Typical velocity-time plots are shown for the three cases in Fig. 4. The log-log plot shows that the steady-state solution for $\Delta > \Delta_c$ is approached quickly. The different slopes for $\Delta = \Delta_c$ and $\Delta < \Delta_c$, corresponding to 0.3- and 0.5-power laws are apparent, as well. The curvature for short times is due to the long initial transient. This curvature means that one must be careful in measuring the slope of the decays. We found it best to plot instead the *derivative* of the log-log plot, giving a time-dependent exponent. (See Fig. 5.) Specifically, we define $\nu(t)$ to be

$$\nu(t) = \frac{d \log_{10} v(t)}{d \log_{10} t} = \frac{t a(t)}{v(t)} \tag{66}$$

where $a(t) = dv/dt$ is the interface acceleration. Figure 5 shows local-exponent plots for undercoolings above, below, and at Δ_c, for $p < p_c$. The topmost curve shows a convergence to a $t^{-\nu}$ power law with $\nu = 1/2$ for $\Delta < \Delta_c$. Other runs, with smaller values of Δ, give even faster convergence to $\nu = 1/2$. The next three lower curves show that as Δ_c is approached from below, the time for the transient to decay to $\nu = 1/2$ diverges. At Δ_c (the dashed line), there is a long plateau at $\nu = 0.306$. However, there is a slight upward curvature for very long times, which is not due to insufficient resolution. Nevertheless, a power law is a good description over at least three decades, even if it is not exact. We also found that for smaller values of p, this transient becomes longer, so that the time interval in which a power law accurately describes the decay will be correspondingly longer, as well. Last, for $\Delta > \Delta_c$, the decay to a steady-state solution ($\nu = 0$) is clearly much faster and sharper than the approach to the $\nu = 1/2$ solution for $\Delta < \Delta_c$. The initial rise to $\nu = 0.3$ reflects the behavior at $\Delta = \Delta_c$.

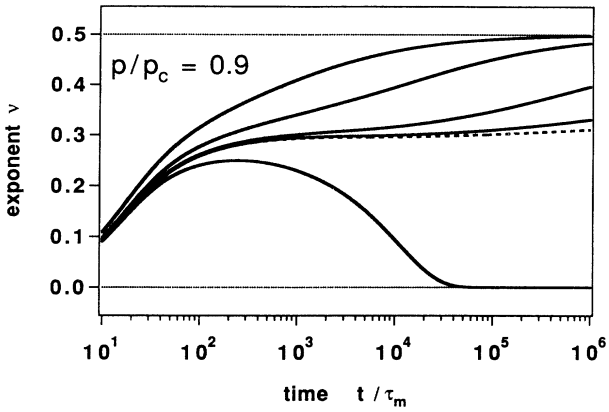

FIG. 5. The evolution of the decay exponent ν for different undercoolings. From top to bottom, the undercoolings are $\Delta/\Delta_c = 0.9240$, 0.9753, 0.9959, 0.9994, 1.000, 1.027. The heavy dashed line is the $\Delta = \Delta_c$ curve. The material parameters are the same as in Fig. 3.

Investigating the approach to steady-state solutions, we plot in Fig. 6 the magnitude of the interface acceleration $a(t)$ versus time t on a semilogarithmic plot. The dashed and dotted curves are for parameters close to the transition to decaying motion. The solid line is at the transition ($\Delta = \Delta_c$, $p = p_c$). When the front velocity approaches a steady-state solution, the acceleration decays exponentially, giving a straight line on the semilogarithmic plot. At the transition, the decay in acceleration follows a power law and is thus curved on this plot. In the steady-state regime, we fit the decay to the form

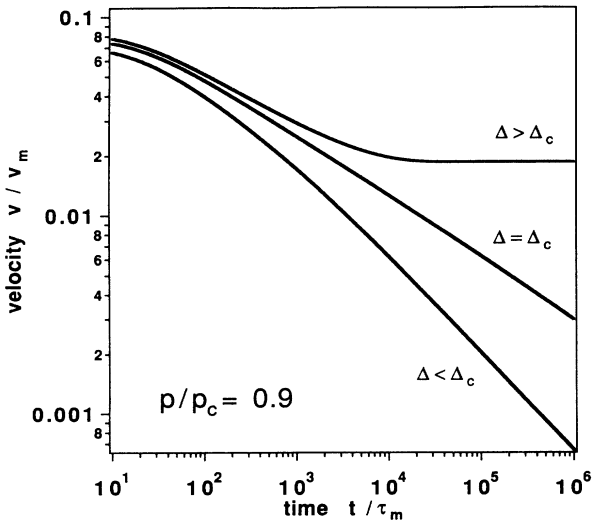

FIG. 4. Evolution of the front velocity with time for three typical cases. The curves are shown on a log-log plot. (1) $\Delta/\Delta_c = 0.92$. The front velocity decays as a power law, according to $t^{-1/2}$. (2) $\Delta = \Delta_c$. The data fall on a straight line with slope $-\nu = -0.306$. (3) $\Delta/\Delta_c = 1.03$. The velocity approaches a constant, steady-state value. The material parameters are $p/p_c = 0.9$ and $\delta = 0.1$.

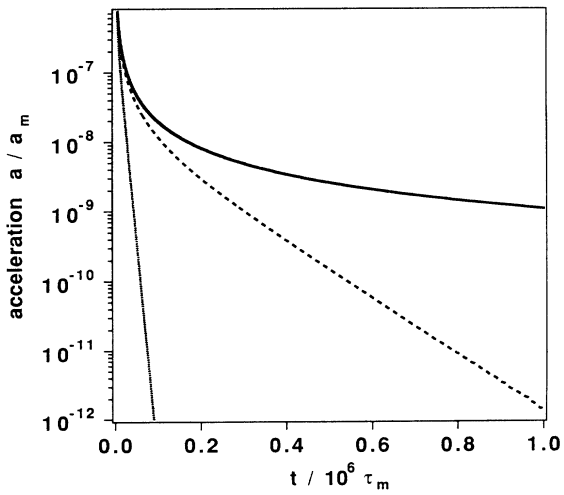

FIG. 6. Decay to steady-state solutions. Acceleration vs time on a semilogarithmic plot. The dotted line is for $p/p_c = 0.9$ and $\Delta/\Delta_c = 1.03$. The dashed line is $p/p_c = 1.1$ and $\Delta = \Delta_c$. Both parameters are close to the transition to decaying motion. The solid line is for $p = p_c$ and $\Delta = \Delta_c$ (just at the transition point). In all cases, $\delta = 0.1$.

$$v(t)=v+Ae^{-t/t_0} . \quad (67)$$

For the dashed curve, $\delta=0.1$, $p/p_c=1.1$, and $\Delta/\Delta_c=1$, and we find $v=1.0\times10^{-2}$, $A=1.7\times10^{-3}$, and $t_0=1.06\times10^{5}$. For the dotted curve, $\delta=0.1$, $p/p_c=0.9$, and $\Delta/\Delta_c=1.03$, and we find $v=1.9\times10^{-2}$, $A=3.8\times10^{-3}$, and $t_0=6.8\times10^{3}$. The long decay times t_0 indicate that we are close to the transition. Far away from the transition, t_0 is of order unity (τ_m). Comparing the dotted and dashed curves, we note that the steady-state velocity v and the amplitude A vary by roughly a factor of 2, while the decay time varies by a factor of about 16. We thus expect that the decay time diverges as the transition is reached.

In the steady-state regime, the u profiles are qualitatively different from those of the decaying regime, as illustrated in Fig. 7. First of all, the u profiles have constant width and do not spread out. Also, away from the transition, the temperature decays over microscopic lengths. The front propagation is thus akin to a temperature shock wave in the kinetics-limited regime. In Fig. 7, we have chosen coexistence boundary conditions, even though $\Delta>\Delta_c$, so that the heat generated at the interface is not enough to heat the liquid back up to coexistence. The boundary conditions thus induce an artificial second front, which becomes broader over time. The width of this second front spreads diffusively via a $t^{1/2}$ power law and the position is fixed near $z=0$, whereas the true front has constant width and travels at constant velocity. Although the boundary conditions are incompatible with steady-state motion, the main front nonetheless moves at constant velocity and contrives to meet the artificial boundary conditions imposed at $z=-\infty$. This strongly suggests that for arbitrary initial conditions, the front travels at constant velocity for long times. In particular, this is the case for a growing germ. In effect, the system picks the correct steady-state boundary conditions dynamically, regardless of the initial conditions.

At $\Delta=\Delta_c$, the behavior depends on p/p_c. As shown in Fig. 8, for $p\le p_c$, the velocity decays via a p-dependent power law. For $p>p_c$, it converges to a steady state. Note that we used the perturbative value of $p_c=2/3\delta$ in calculating p/p_c. (We used $\delta=0.1$, a value well within the range of validity of the perturbation expansion for p_c; see [10].) The velocity-decay exponents ν, obtained from least-squares fits, are shown in Fig. 9 for six different values of p/p_c. The dashed line represents the transition to steady-state motion at p_c. Note that ν does not go to 0 at p_c. For small values of p/p_c, ν varies little. Our measurements of ν are to be compared with the prediction of Oswald for the diffusive model with linear kinetics: $\nu=1/3$. Although the two values are compatible in the limit $p/p_c\to0$, we find that ν depends slightly on p and δ. Either this dependence implies that ν is nonuniversal, or we are not yet in the asymptotic regime. If the latter is true, the initial transients are extremely long lived, and

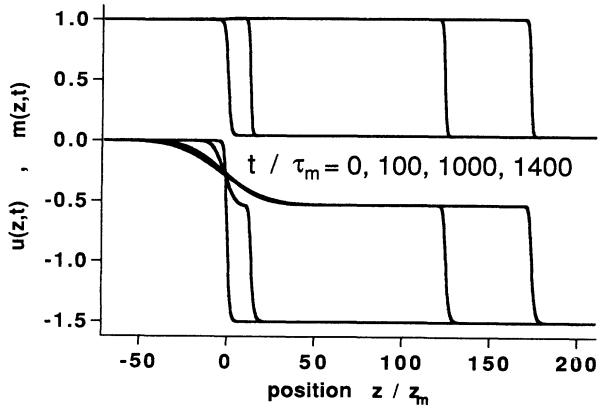

FIG. 7. Same as Fig. 2: Time evolution of $m(z,t)$ and $u(z,t)$ in the steady-state regime $\Delta/\Delta_c=1.54$. The material parameters are $p/p_c=0.5$ and $\delta=0.1$. Although the boundary conditions force $m_-=1.0$ and $u_-=0$, the leading edges of the u and m profiles evolve at constant velocity.

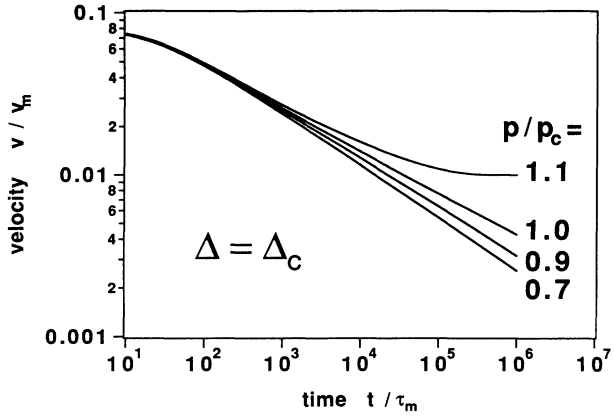

FIG. 8. Velocity-time plot for $\Delta=\Delta_c$ and $\delta=0.1$ and for different p/p_c, as indicated.

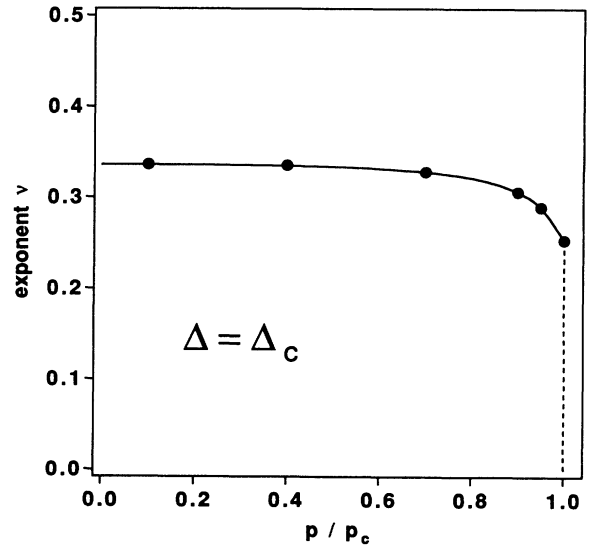

FIG. 9. Fitted decay exponents ν vs p/p_c for $\Delta=\Delta_c$ and $\delta=0.1$. The lines are guides for the eye. The dashed line represents the transition from power-law decay to steady-state motion that occurs for $p>p_c$.

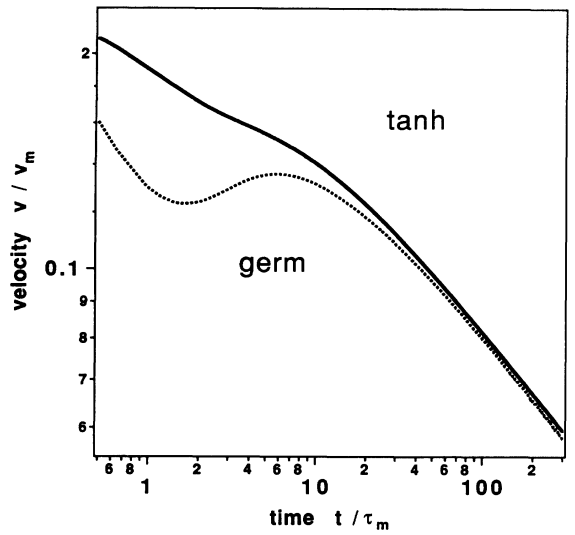

FIG. 10. Velocity-time plot for two different initial conditions showing convergence to same decay exponent. The solid line represents a tanh-like initial profile, while the dashed line represents a Gaussian germ. The material parameters are $p/p_c=0.9$ and $\delta=0.2$. The undercooling is $\Delta=\Delta_c$.

real experiments may not attain the asymptotic regime, either.

We checked that the decay exponent ν is the same for tanh and germ initial conditions. See Fig. 10. Again, this strongly suggests that decay exponents are independent of initial conditions.

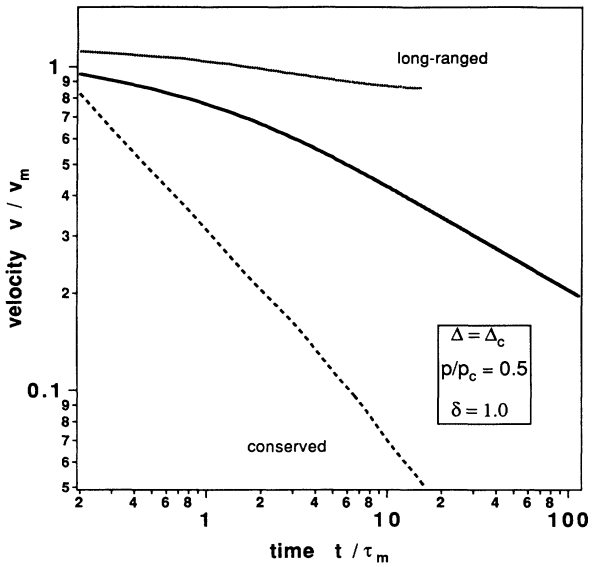

FIG. 11. Log-log plot of the interface velocity vs time in the parabolic model. The initial profile was a quasi sharp kink. The solid line shows, for reference, the case of the nonconserved order parameter with short-range forces, the focus of our paper. The material parameters and undercooling are given on the figure. The dotted line shows, for the same parameters, the effects of long-range forces. The parameters for the long-range potential are $\alpha=0.25$ and $\xi=4$. The dashed line shows the effect of having a conserved order parameter.

Finally, when $p>p_c$, stable steady-state solutions exist over a small range $\bar{\Delta}_c<\Delta<\Delta_c$, consistent with [14]. This is interesting because the steady-state, $\Delta<\Delta_c$ solution implies that the solid created dynamically is superheated: Ordinarily, the solid created is at either coexistence or at a lower temperature. We have checked that even if we impose coexistence or germ boundary conditions, we get a superheated solid. For $\Delta=\bar{\Delta}_c$, the solution jumps from a finite-velocity, steady state to a $t^{-1/2}$ solution. The analytic form of these superheated, constant-velocity solutions and the scaling of v near $\bar{\Delta}_c$ were derived for the parabolic model in [14].

These simulations of the Ginzburg-Landau model were compared with velocity-decay laws of the parabolic model, obtained by the method described in Sec. III B. A typical example is shown as the solid curve in Fig. 11. Although we could not follow solutions as far as we did in the Ginzburg-Landau case, we nonetheless found similar results. In the next section, we shall discuss modifications of the parabolic model to include long-range forces and conserved order-parameter dynamics.

V. INFLUENCE OF LONG-RANGE FORCES AND CONSERVED ORDER-PARAMETER DYNAMICS

A. Long-range forces

We now discuss the influence that long-range forces exert on the dynamics of the parabolic model. Long-range forces such as van der Waals interactions are conveniently described by adding [26]

$$F_l=-\tfrac{1}{4}\int_{-\infty}^{\infty}dz\int_{-\infty}^{\infty}dz'w(|z-z'|)[m(z,t)-m(z',t)]^2 \tag{68}$$

to the free-energy functional (3). If m represents the density, $w(z)$ is the parallel-integrated, long-range tail of the microscopic interparticle potential [23]. Since the extra term in Eq. (68) is diagonal in Fourier space, we can easily incorporate long-range interactions into our formalism for the parabolic model. To proceed, we note that the only change in the equations given in Sec. III B is in the matrix $\underline{C}_K$ [see Eq. (55)], which is replaced by

$$\underline{C}_K=-\begin{bmatrix} K^2/2p+\frac{1}{2}\delta & \frac{1}{2}K^2+1+W(K) \\ \frac{1}{2}\delta & \frac{1}{2}K^2+1+W(K)\end{bmatrix} \tag{69}$$

where $W(K)=[w(K)-w(0)]\sqrt{2\pi}$ and $w(K)$ is the Fourier transform of $w(z)$, as defined in Eq. (54). For concreteness, we choose the attractive inverse-power potential

$$w(z)=-\frac{2\alpha\xi}{\sqrt{2\pi}(\xi^2+z^2)}\sim\frac{1}{z^2}\quad(z\to\infty)\,. \tag{70}$$

The coupling parameter for the long-range potential is chosen to be rather large so that effects stemming from long-range potentials are clearly visible. We note that for our phase-diffusion model, much less is known analytically about the effect of long-range forces than is known about short-range forces. For example, for $\Delta=\Delta_c$, we

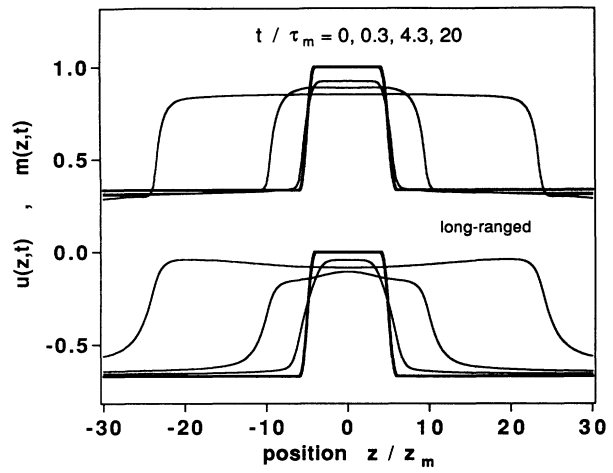

FIG. 12. Time evolution of interface profiles when long-range forces are included. The parameters are listed in Fig. 10.

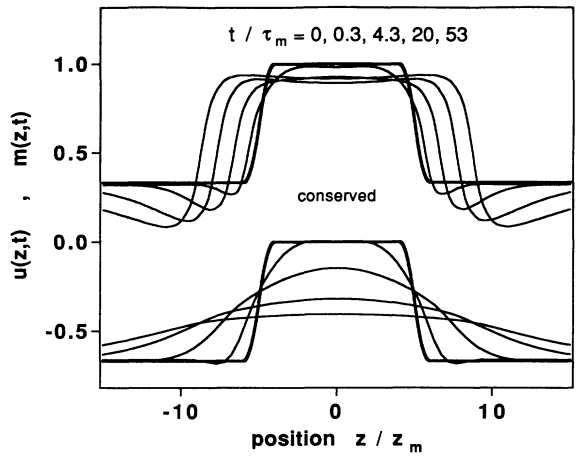

FIG. 13. Time evolution of interface profiles for nonconserved order-parameter dynamics. The parameters are listed in Fig. 10.

cannot calculate $p_c(\delta)$ analytically. In Fig. 11, the interface velocity is enhanced considerably compared to the short-range case and tends to a finite steady-state velocity. This shows that p_c is reduced when attractive, long-range forces are present.

The acceleration of interface growth in the presence of long-range, attractive forces is analogous to that observed in the width of liquid layers in simple models of surface melting [27].

For $p < p_c$ and $\Delta = \Delta_c$, in Fig. 12, we show the evolution of the order-parameter and temperature profiles under the same conditions as in Fig. 11. The long-range forces modify the shapes of the tails of the interface profiles: they are now power laws, with a slower decay than the exponentials one finds in the short-range case.

B. Conserved order-parameter dynamics

We have heretofore assumed that the order parameter distinguished the two phases was not conserved. If, however, it is conserved, then the equation of motion Eq. (2) is replaced by [1]

$$\frac{\partial m}{\partial t} = -\frac{\partial^2}{\partial z^2}\left[\tilde{\Gamma}\frac{\partial F}{\delta m}\right] . \tag{71}$$

This means that Eq. (55) must be modified to read

$$\underline{C}_K = -\begin{bmatrix} K^2/2p + \frac{1}{2}K^2\delta & K^2(\frac{1}{2}K^2+1) \\ \frac{1}{2}K^2\delta & K^2(\frac{1}{2}K^2+1) \end{bmatrix} . \tag{72}$$

The natural time units must also be changed accordingly, to $\tau_m = l_m^2/(\lambda\tilde{\Gamma})$. Finally, the term $\sin Kz_0(t')/K$ in Eq. (53) becomes $K\sin Kz_0(t')$. Interfacial profiles are shown in Fig. 13. Because m is conserved, interface motion implies that quantities of m must diffuse from the liquid to the solid, hindering growth. The dashed line in Fig. 11 shows the interface-velocity decay in the conserved case. The growth velocity of the ordered phase slows much more quickly than for the nonconserved case (shown as a solid line), where the same values of δ, p, and Δ were used. Indeed, if the spatial domain of the solid that is studied is finite (as it is in our simulations), the global conservation of m implies that only a finite fraction of the domain can crystallize, even after the temperature field u has decayed to a uniform value. If one interprets the conserved m, for example, as a concentration of impurities, then this situation merely restates the well-known fact that impure materials have a finite temperature range over which solid and liquid phases coexist.

Since both m and u are conserved and governed by diffusionlike equations, interesting dynamics will result only if the effective diffusion constants for the two quantities are of comparable magnitude. Otherwise, the dynamics of the more rapidly diffusing field will be slaved adiabatically to the dynamics of the more slowly diffusing field, and the interface motion will be correspondingly simpler.

VI. EXPERIMENTAL CONSEQUENCES

The two qualitatively new features arising from our simulations are the approximate, p- and δ-dependent 0.3-power-law decay at $\Delta = \Delta_c$ and the jump from a nonzero velocity steady-state solution to a diffusive solution when $p > p_c$. Both occur, as suggested in Sec. II A, near Δ_c, where the diffusive, $t^{-1/2}$ regime crosses over to a kinetic, steady-state regime.

A. Estimates of typical materials parameters

For concreteness, we look at a representative metal, an organic solid, and a liquid crystal for both the thermal model (pure material) and the chemical model (impurities added deliberately). In Table I, we collect data for pure nickel, a nickel-copper alloy, pure succinonitrile, succinonitrile plus acetone, the pure liquid crystal 4,4′-*n*-octylcyanobiphenyl (8CB) (nematic-isotropic transition),

TABLE I. Material parameters for six different systems, representing typical pure and impure metals, dendrite-forming organic solids, and liquid-crystalline mesophases. SCN denotes succinonitrile, AC denotes acetone, 8CB denotes 4,4′-*n*-octylcyanobiphenyl, and Hex. denotes hexachloroethane. The molecular weight given for the alloy systems is that of the added impurity. The diffusivity D is the heat and mass diffusivity for the thermal and chemical cases, respectively. For pure materials, the "unit Δ" is L/c_p. For alloys, it is given by $(dT/dC)C_0(1-k)/k$. In the alloy case, δ is evaluated at unit undercooling.

	Ni	$Ni_{30}Cu_{70}$	SCN	SCN+AC	8CB	8CB+Hex.
References	[34]	[34]	[35]	[36]	[37]	[37]
M_w (g/mol)	58.7	63.5	80.092	58.08	291.2	236.74
ρ_{liq} (g/cm^3)	7.8		1.0		0.979	
T_0 (K)	1726		331.24		313.5	
L (10^9 erg/mol)	172	136	37		6.12	
c_p (10^9 erg/mol K)	0.43		1.6		7.3	
σ (erg/cm^2)	464		8.94		0.0094	
z_m (10^{-8} cm)	2.3		5.1		100	
$\sigma M_w/\rho_{liq}L$ (10^{-8}cm)	2.0		1.94		0.0046	
β (cm/sec K)	160		20		0.01	
D (10^{-5} cm^2/sec)	6500	6	1150	1.27	60	0.038
dT/dc (K/mol %)		4.38		3.86		1.35
k		0.81		0.1		0.85
c_0 (mol %)		70		0.1→10		0.1→10
unit Δ (K)	397	72	23.1	2.5→252	0.84	0.024→2.4
δ	0.088	0.016	0.062	0.0067→0.67	1.96	0.31→31
p/p_c	0.012	2.3	0.015	0.145→14.5	7.3×10^{-6}	0.000 13→0.013

and 8CB doped with hexachloroethane. The parameters δ and p, defined for the thermal case in Eqs. (6) and (11) and for the chemical case in Eqs. (25)–(27), require some care to estimate since λ and Γ are hard to measure directly. The trick is to relate them to the surface tension and the kinetic coefficient (β), which are more easily measured. The equilibrium surface tension σ is obtained by solving Eq. (3) at $u=0$ and evaluating $\int (m_z)^2 dz$. We find, in real units,

$$\frac{\sigma M_W}{\rho_0 k_B T_0} = \frac{\lambda \xi_m}{6} \tag{73}$$

where ρ_0 is the density at coexistence and M_W is the molecular weight. (We are assuming both phases have equal density.) From σ, we can estimate δ. We find, following roughly the calculation given already in Schofield and Oxtoby [12], that

$$\delta = \frac{1}{3}\frac{z_m}{\sigma M_W/\rho_0 L}\frac{L/c_p}{T_0} . \tag{74}$$

To estimate Γ, we calculate the kinetic undercooling developed by constant-velocity fronts:

$$v \approx -\sqrt{2}\delta u \frac{\xi_m}{\tau_m} = \frac{\xi_m}{\tau_m}\delta\frac{T_0-T}{L/c_p} . \tag{75}$$

This is to be compared with the standard definition of the kinetic coefficient $v=\beta(T_0-T)$ [28]. One finds for Γ, then,

$$\Gamma = \frac{\lambda}{2\sqrt{2}}\frac{\beta T_0}{z_m}\frac{k_B T_0}{L} . \tag{76}$$

The estimate of Γ then leads to an estimate of p via the definition in Sec. II A.

The above estimates are for the thermal model. To calculate the corresponding coefficients in the chemical case, we note that $L/c_p \to (dT/dC)C_0(1/k-1)$ and $D_T \to D_C$. As mentioned earlier, since one can set C_0 easily, one can effectively tune δ. Thus in the table the ranges of values shown reflect the range of C_0 that one may easily have (0.1–10 mol %). Also, the large values of p reflect the fact that $D_T/D_C \approx 100-1000$, typically.

Although the estimates in Table I were done carefully, the actual values should be used with caution since β and z_m are poorly measured or can only be estimated. The latter can be measured accurately should the need exist. The former is hard to measure experimentally. (A useful method to measure β in metals has recently been developed by Rodway and Hunt [29].)

Scanning the values of δ and p/p_c for different materials, a number of conclusions emerge. First of all, metals and organic crystals have rather similar parameter values, whereas the liquid-crystal values are quite different. We conclude that the scale of δ and p/p_c is set mainly by the strength of the first-order transition. True solid-liquid transitions will have comparable p's and δ's, while weak mesophase transitions have very small p's because the microscopic length and time scales are beginning to become large. We have also estimated the parameter values of lead, xenon, and a discotic-liquid mesophase transition and find p's and δ's in accordance with the above discussion.

B. Suggestions for observing the anomalous exponent and velocity jump

For the typical pure solid-liquid transition, the coupling δ is small, as is p/p_c. Thus one can observe the 0.3 exponent but not the jump in such materials. The chemi-

cal version of the solid-liquid transition allows one to tune δ and p/p_c so that one might indeed be able to cross from $p<p_c$ to $p>p_c$ in a single system merely by varying the concentration of impurity. Referring to (26), we note that $(2/\lambda)(L/k_BT_0)$ is a number of order unity. Thus in the chemical model $\delta\approx\Delta T/T_0$, where ΔT is the melting range (liquidus minus solidus) at the sample concentration C_0. A small ΔT implies a large undercooling Δ. Observing the 0.3 exponent should then be easier in the chemical case than it is in the thermal case. On the other hand, since $p_c\approx 2/(3\delta)\approx 2/(3\Delta T/T_0)$, a large ΔT may be needed to have $p>p_c$. But if ΔT is large, then it will be difficult to undercool the liquid to $\Delta=1$ without spontaneous nucleation occurring throughout the liquid. For the ordinary liquid-solid transitions examined in Table I, the case $p>p_c$ may be challenging to observe, although the values for succinonitrile-acetone do not rule out seeing the velocity jump.

We note that the mesophase example requires further thought. The values of δ in both the thermal and especially the chemical case are very large. The simple form we took in Eq. (4) above implicitly assumed a small δ, since the $(\delta/2)um$ term is the first term of an expansion. Thus, although the liquid-crystal case is interesting, more work needs to be done to understand the implications of the phase-field model in this case.

To observe the anomalous 0.3 exponent, we must determine the width of the crossover near $\Delta=\Delta_c$. In principle, one could investigate the behavior as $\Delta\rightarrow\Delta_c$ from above or from below. When $\Delta\rightarrow\Delta_c$ from below, one observes a crossover from a 0.3-power law to a 0.5-power law. Since the difference in the exponents is small and the crossover time τ^* long, this is hard to observe numerically and would also be hard to observe experimentally. By contrast, when one approaches Δ_c from above, the velocity decays *exponentially* to the steady-state value. A log-log plot then shows a clear, sharp crossover time, as illustrated in Fig. 4. Thus it should be easier to prove the existence of the anomalous exponent by looking at transients to steady-state fronts.

The crossover times may be estimated by extrapolating numerical results for the power-law part of the decay to meet the line tangent to the steady-state part of the velocity-time log-log curve. In practice, even our long-time simulations correspond to very short experimental times. Typically, $\tau_m\approx 10^{-12}-10^{-10}$ sec, so that in order to compare simulation times to experimental times, we would need to continue the simulations to times of order $10^{10}\tau_m$. On the other hand, most of our interesting results at Δ_c were shown for $p/p_c=0.9$. The apparent τ^* in Fig. 5 (of order $t=5\times 10^4$) will be greatly enhanced for smaller values of p/p_c. Our simulations cannot show the steady-state velocity crossover for smaller values of p/p_c because that time rapidly becomes longer than the maximum time we can run our program. We can nonetheless estimate this time by observing the power-law-decay transient for small p/p_c at $\Delta=\Delta_c$. For $\Delta\approx\Delta_c$, this decay does not change very much, and we shall use the value at Δ_c. We then extrapolate the velocity-decay curve to the known steady-state velocity corresponding to the value of $\Delta>\Delta_c$ in which we are interested. This defines τ^*. The steady-state velocity is known exactly in the parabolic model and approximately in the Ginzburg-Landau model. In the parabolic model, the relation is $v=\sqrt{2}\delta(\Delta-\Delta_c)/(1-p/p_c)$ [14]. As an example, for $p/p_c=0.1$, $\delta=0.1$, and $\Delta-\Delta_c=0.001$ (the experimental limit achievable for pure succinonitrile, for example) $\tau^*\approx 10^{11}$, in units of τ_m. For succinonitrile, this corresponds to a few seconds.

C. The Mullins-Sekerka instability

Our calculation is limited to one dimension, while most experiments have two- or three-dimensional geometries. In higher dimensions, line or surface tension will be present, but their effects will be small once the germ's radius is much bigger than z_m. A more serious worry is whether the Mullins-Sekerka instability [30] will destablize the interface and obscure the solutions we have been studying. In the diffusive regime, the instability will certainly be present, and a germ will evolve into dendrites whose tips move at constant velocity. At the large undercoolings considered in this paper, calculations based strictly on the diffusive model with linear kinetics imply that for $\Delta<\Delta_s=1+D_TL/\beta T_0\sigma$ [where the front velocity $v_{MS}=D_TL^2/(c_pT_0\sigma)$], a flat interface ripples via the Mullins-Sekerka mechanism [16,17]. The experimental scenario is that a crystal initially freezes fairly rapidly and then slows down. If its asymptotic velocity is greater than v_{MS}, the front will be stable. If not, the Mullins-Sekerka instability will set in once the front slows down below v_{MS}.

Our calculations would seem to be valid for circular or spherical germs only until the front destabilizes. However, if instead of measuring the interface position as a function of time, we measure the total amount of solid created (the area in $d=2$, the volume $d=3$), then the effect of the Mullins-Sekerka instability is less clear. First of all, when the amplitude of the instability is small compared to the germ radius, there will likely be little change to the area or volume measurement compared to the unstabilized germ. The reason is that for short times, only a few discrete modes will grow. Since the shape is a sum of growing sine waves, the area or volume will be unaffected for sufficiently small amplitudes of the instability. Even when the amplitude is large, the overall area or velocity scaling may be unchanged. In the diffusion-limited regime, the complicated dendritic patterns are transient, the final state being a system that has been converted from liquid to solid. Since heat (or impurities) diffuse out to infinity, we expect that the area or volume time scalings will remain diffusive.

Experimentally, it would thus be interesting to measure the evolution of area or volume versus time in both the dendritic and steady-state regimes. If the time scaling changes in the dendritic regime, then the Mullins-Sekerka instability would act as a kind of hyperdiffusive mechanism that transports heat out to infinity qualitatively faster than via diffusion alone. The point has not yet been studied in detail, but measurements on liquid

crystals by Oswald, Malthête, and Pelcé [31] suggest that the area of two-dimensional germs does grow linearly with time, even when their shape is highly dendritic.

Should crystal growth in the presence of the dendrites obey diffusive scalings, then the classification of long-time solutions to the equations of crystal growth discussed in this paper would be expected to hold independently of the existence of the Mullins-Sekerka instability. Should, by contrast, there be qualitative changes in the area-time or volume-time plots within the diffusive regime, that would still be an interesting and perhaps fruitful way of characterizing solidification process that would complement measurements of dendrite tip velocities, which heretofore have been the focus of much of the theoretical and experimental work on solidification. In any case, the measurement is straightforward with modern image-processing techniques, and there clearly must be some kind of transition, since in the kinetics-dominated regime, the shape will be circular (area proportional to t^2) or spherical (volume proportional to t^3).

To conclude on an even more speculative note, an outstanding problem of crystallization and diffusion-limited growth processes in general is the existence of so-called dense-branched morphologies [32]. Is the dense-branched regime merely the destablized version of the constant-velocity solution? Qualitatively, the argument is plausible. Again, the most extensive observations are by Oswald, Malthête, and Pelcé [31], who examined the growth of an impure liquid crystal (discotic phase growing into liquid phase). For $\Delta < 0.6$, they observe petal-shaped and dendritic regimes, where the area grows linearly with time. For $\Delta > 0.6$, they observe a dense-branched regime. They do not give measurements of the area versus time in this regime, but the photographs shown in their article suggest that the area grows faster than linearly with time. If the area grows quadratically with time, then one would be tempted to conclude that the germ is already in the kinetic regime, although it was still unstable to the Mullins-Sekerka mechanism.

Finally, recent work by Geminard and Oswald [33] on purer samples suggests a $t^{-1/2}$ solution for $\Delta \lesssim 0.3$ and a constant-velocity solution for $\Delta \gtrsim 0.5$. As the experiments are still preliminary, we note only that three-dimensional effects (the curvature of the meniscus that occurs when a sample is enclosed in a narrow space between two glass plates) may be important.

VII. CONCLUSIONS

We have extensively studied numerically the one-dimensional phase-field model as a function of material parameters and undercooling and have found, in addition to the known diffusive and kinetic regimes, two new effects. At unit undercooling, the front velocity decay is very well approximated by a p- and δ-dependent power law $t^{-\nu}$, with $\nu \approx 0.3$. For $\delta \to 0$ and $p/p_c \to 0$, our results are compatible with the $\nu = 1/3$ exponent from Oswald's impurity-conservation argument. For other p's and δ's, we may conclude either that ν depends weakly on p and δ or that we have not yet reached the true asymptotic regime; however, the long transients imply that experiments may not reach the regime, either. For small diffusivities (most likely mass diffusivities), we predict a jump from finite-velocity solutions to diffusive solutions. Estimates of material parameters show that both of these new effects should be observable in experiments.

Although our calculations are for one-dimensional systems, our classification of asymptotic behavior may apply to two- and three-dimensional geometries, even in the presence of the Mullins-Sekerka instability. We have also speculated that the transition from dendritic to dense-branched morphology reflects the transition from diffusive to kinetic growth. As always, the key point is whether heat or impurities can remain where they are released or whether they must be transported out to infinity.

ACKNOWLEDGMENTS

This work was begun while the authors were at the Ecole Normale Supérieure de Lyon, in Lyon, France. We are grateful to Patrick Oswald for discussing unpublished results with us and for allowing us to reproduce his argument on the anomalous exponent in advance of publication. We thank Michael Marder for helpful suggestions. H. L. acknowledges financial support by the "Deutsche Forschungsgemeinschaft." J.B. was supported by an operating grant from the National Science and Engineering Research Council of Canada. L.S.T. was supported by a Chaire Louis Néel and by NSF Grant No. DMS-8901767. Computing resources were provided by the University of Texas System Center for High-Performance Computing.

[1] See, for example, P. R. Harrowell and D. W. Oxtoby, J. Chem. Phys. **86**, 2932 (1987).

[2] D. W. Oxtoby, in *Liquids, Freezing, and the Glass Transition,* edited by J.-P. Hansen, D. Levesque, and J. Zinn-Justin (North-Holland, Amsterdam, 1991).

[3] M. E. Glicksman and R. J. Schaefer, J. Cryst. Growth **1**, 297 (1969); R. J. Schaefer and M. E. Glicksman, J. Cryst. Growth **5**, 44 (1969).

[4] J. S. Langer, in *Chance and Matter,* Proceedings of the Les Houches Summer School, Session XLVI, edited by J. Souletie, J. Vannimenus, and R. Stora (Elsevier, Amsterdam, 1987).

[5] B. I. Halperin, P. C. Hohenberg, and S.-K. Ma, Phys. Rev. B **10**, 139 (1974).

[6] P. C. Hohenberg and B. I. Halperin, Rev. Mod. Phys. **49**, 435 (1977).

[7] J. B. Collins and H. Levine, Phys. Rev. B **31**, 6119 (1985).

[8] J. B. Collins, A. Chakrabarti, and J. D. Gunton, Phys. Rev. B **39**, 1506 (1989).

[9] J. S. Langer, in *Directions in Condensed Matter Physics,* edited by G. Grinstein and G. Mazenko (World Scientific, Singapore, 1986), p. 165.

[10] G. Caginalp, Carnegie-Mellon Research Report No. 82-5 (1982); G. Caginalp, in *Applications of Field Theory to Sta-*

tistical Mechanics, edited by L. Garrido, Lecture Notes in Physics Vol. 216 (Springer-Verlag, Berlin, 1984), p. 216.
[11] F. Liu and N. Goldenfeld, Phys. Rev. A **42**, 895 (1990).
[12] S. A. Schofield and D. W. Oxtoby, J. Chem. Phys. **94**, 2176 (1991).
[13] H. Löwen, S. A. Schofield, and D. W. Oxtoby, J. Chem. Phys. **94**, 5685 (1991).
[14] H. Löwen and J. Bechhoefer, Europhys. Lett. **16**, 195 (1991).
[15] C. Zener, J. Appl. Phys. **20**, 950 (1949).
[16] E. A. Brener and D. E. Temkin, Europhys. Lett. **10**, 171 (1989).
[17] C. Misbah, H. Müller-Krumbhaar, and D. E. Temkin, J. Phys. (Paris) I **1**, 585 (1991).
[18] P. Oswald (private communication).
[19] G. Caginalp, Phys. Rev. A **39**, 5887 (1989).
[20] G. Fix, in *Free Boundary Problems,* edited by A. Fasano and M. Primicerio (Pittman, London, 1983), pp. 580–589.
[21] D. P. Woodruff, *The Solid-Liquid Interface* (Cambridge University Press, Cambridge, England, 1973).
[22] J. S. Langer, Rev. Mod. Phys. **52**, 1 (1980).
[23] R. W. Metcalfe, S. A. Orszag, M.E. Brachet, S. Menon, and J. J. Riley, J. Fluid Mech. **184**, 207 (1987).
[24] H. Löwen and D. W. Oxtoby, J. Chem. Phys. **93**, 674 (1990).
[25] H. Löwen, T. Beier, and H. Wagner, Europhys. Lett. **9**, 791 (1989); Z. Phys. B **79**, 109 (1990).
[26] R. Lipowsky, Z. Phys. B **55**, 335 (1984); **55**, 345 (1984).
[27] R. Lipowsky, J. Phys. A **18**, L585 (1985).
[28] The expression for β is very close to a recent estimate, $v=(k_B T_0/M)^{1/2}(T_0-T)/T_0$, obtained from the density-functional theory of freezing. M is the mass of an atom and $(k_B T_0/M)^{1/2}$ is a thermal velocity $\approx \xi_m/\tau_m$. See L. V. Mikheev and A. A. Chernov, J. Cryst. Growth **112**, 591 (1991).
[29] G. H. Rodway and J. D. Hunt, J. Cryst. Growth **112**, 554 (1991).
[30] W. W. Mullins and R. F. Sekerka, J. Appl. Phys. **35**, 444 (1963).
[31] P. Oswald, J. Malthête, and P. Pelcé, J. Phys. (Paris) **50**, 2121 (1989).
[32] G. Deutscher, in *Random Fluctuations and Pattern Growth: Experiments and Models,* edited by H. E. Stanley and N. Ostrowsky (Kluwer, Dordrecht, 1988), p. 117. A different explanation of dense-branched morphology (DBM) has been proposed by F. Liu and N. Goldenfeld, Phys. Rev. A **42**, 5052 (1990). Goldenfeld's original discussion of DBM, given in the context of spherulitic growth of polymers, is actually closer in spirit to our mechanism than is the more precise mechanism described in the reference above. For the original discussion, see N. Goldenfeld, J. Cryst. Growth **84**, 601 (1987).
[33] J.-C. Geminard and P. Oswald (unpublished).
[34] R. Willnecker, D. M. Herlach, and B. Feuerbacher, Phys. Rev. Lett. **62**, 2707 (1989).
[35] M. E. Glicksman, R. J. Schaefer, and J. D. Ayers, Metall. Trans. A **7**, 1747 (1976).
[36] M. A. Chopra, M. E. Glicksman, and N. B. Singh, J. Cryst. Growth **92**, 543 (1988), and references therein.
[37] J. Bechhoefer, A. J. Simon, A. Libchaber, and P. Oswald, Phys. Rev. A **40**, 2042 (1989).